Mem. S.A.It. Suppl. Vol. 17, 24
© SAIt 2011
**Memorie** della
**Supplementi**

# Simulating the WFXT sky

P. Tozzi[1,2], J. Santos[1], H. Yu[1], A. Bignamini[3], P. Rosati[4], S. Borgani[2,3], S. Campana[5], P. Conconi[5], R. Gilli[6], M. Paolillo[7], A. Ptak[8], and the WFXT Team

[1] INAF – OATs, Via Tiepolo 11, I-34131 Trieste, Italy e-mail: tozzi@oats.inaf.it
[2] INFN Trieste, via Valerio 2, I-34127 Trieste, Italy
[3] Dipartimento di Fisica, Università di Trieste, via Tiepolo 11, I-34143 Trieste, Italy
[4] ESO - European Southern Observatory, D-85748 Garching bei Munchen, Germany
[5] INAF - OABrera, via Brera 28, 20121 Milano, Italy
[6] INAF - OABo, via Ranzani 1, I-40127 Bologna, Italy
[7] Università Federico II, Dip. di Scienze Fisiche, via Cintia, I-80126, Napoli
[8] NASA Goddard Space Flight Center, Maryland, USA

**Abstract.** We investigate the scientific impact of the Wide Field X-ray Telescope mission. We present simulated images and spectra of X–ray sources as observed from the three surveys planned for the nominal 5-year WFXT lifetime. The goal of these simulations is to provide WFXT images of the extragalactic sky in different energy bands based on accurate description of AGN populations, normal and star forming galaxies, groups and clusters of galaxies. The images are realized using a detailed PSF model, instrumental and physical backgrounds/foregrounds, accurate model of the effective area and the related vignetting effect. The simulated images can be used to evaluate the flux limits for detection of point and extended sources, the effect of source confusion at very faint fluxes, and in general the efficiency of detection algorithms. We also simulate the spectra of the detected sources, in order to address specific science topics which are unique to WFXT. Among them, we focus on the characterization of the Intra Cluster Medium (ICM) of high-z clusters, and in particular on the measurement of the redshift from the ICM spectrum in order to build a cosmological sample of galaxy clusters. The end-to-end simulation procedure presented here, is a valuable tool in optimizing the mission design, characterizing the WFXT discovery space and verifying the connection between mission requirements and scientific goals. Thanks to this effort, we can conclude on firm basis that an X-ray mission optimized for surveys like WFXT is necessary to bring X-ray astronomy at the level of the optical, IR, submm and radio wavebands as foreseen in the coming decade.

**Key words.** Cosmology: galaxy clusters; AGN: observations - X-rays: surveys

## 1. Introduction

The strong interest behind the Wide Field X–ray Telescope (WFXT) stems from the fact that no planned or foreseen X-ray mission is optimally designed for surveys. The tremendous scientific impact that we experienced in the last ten years thanks to the Chandra and XMM-Newton X-ray telescopes, largely relies on the previous all–sky surveys performed by satel-

*Send offprint requests to*: P. Tozzi

lites like Einstein or ROSAT, which were able to provide a large number of potentially interesting X-ray targets. A new, deeper, wide-angle X-ray survey is needed in order to perform a significant step forward in the field of X-ray astronomy. In addition, the innovative concept of WFXT (Murray et al. 2008)[1] will allow one not only to deliver catalogs of X-ray sources, but also to characterize most of them, and achieve several scientific goals well in advance of a multiwavelength follow-up. Eventually, the synergies with future surveys in other wavebands will greatly enhance its scientific impact (see Rosati et al. this volume). In our view, the WFXT mission will provide an immense legacy value for Galactic and extragalactic astronomy.

Simulations of data products from the planned WFXT surveys are crucial in order to quantify the scientific impact of the mission. In order to achieve this goal, we set up a procedure to build images of extragalactic fields and spectra of the sources according to the instrument design of WFXT. We put a strong effort in the modelization of the X-ray source populations, in order to investigate in detail several science cases which are unique to WFXT. Among these scientific cases we discuss the study of the ICM in groups and clusters of galaxies, the building of a cosmological sample of clusters whose redshift is obtained directly by the X-ray spectral analysis, and the characterization of the different classes of AGN up to redshift $z \sim 6$ (Giacconi et al. 2009; Murray et al. 2009; Vikhlinin et al. 2009). Many other science cases can be addressed with these simulations, including cases relevant for Galactic astronomy and the local Universe (Ptak et al. 2009), but are not discussed here.

This paper is organized as follows. In §2 we derive the main quantities which are relevant to the simulations like the background and foreground components and the typical conversion factors, and show how we build a mock WFXT image. In §3 we describe the modelization of the extragalactic source populations adopted in our simulations. In §4 we describe the results of a preliminary analysis using a simple detection algorithm to provide a conservative estimate of the capability of WFXT of detecting X-ray sources. In §5 we describe the spectral simulations and focus on the capability of measuring the redshift for a large sample of groups and clusters of galaxies. Finally our conclusions are summarized in §6.

[1] http://www.wfxt.eu; http://wfxt.pha.jhu.edu

## 2. Building WFXT simulated images

The details of the WFXT design are presented in the contribution by Pareschi & Campana in this volume. Here we recall the most relevant properties which affect our simulations. First we consider the sensitivity of the X-ray telescope. The total effective area of the three modules of the WFXT at the aimpoint is shown in Figure 1. In the soft band, the effective area of WFXT is about one order of magnitude larger than the total effective area of XMM (the sum of the PN and the two MOS), and about two orders of magnitudes larger than the Chandra one. The effective area in the hard band is comparable to the total value of XMM at 5 keV. Achieving a large effective area in the soft band while still keeping a significant area in the hard band (2-7 keV) is key to characterize the detected sources.

With its very large field of view (1 square degree), WFXT images suffer an important vignetting effect, which consists in a decrease of the effective area with the off–axis angle with respect to the aimpoint (assumed to be in the center of the image). This is an important aspect to be included in the simulations, since it allows us to compute correctly the number of detected photons for the sources randomly distributed in the field. The vignetting in both bands for a single pointing is shown in Figure 2.

The spectral resolution, defined as $E/\Delta E$, where $\Delta E$ is the Half Energy Width (HEW) of an emission line with zero intrinsic width, is shown in Figure 3. Spectral resolution is about a factor of 3 better than the Chandra (ACIS-I) resolution over the whole energy band, while it is comparable to the XMM resolution (PN) above 1 keV. Spectral resolution is crucial to perform line diagnostic. As we will see, the

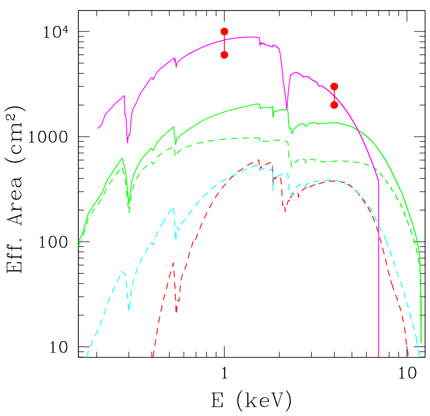


**Fig. 1.** Effective area for WFXT design (magenta) at the aimpoint for the sum of the three modules. Red dots show the requirement and the goal at 1 and 4 keV. The *Chandra* effective area is shown as a red dashed line, while the total XMM-Newton response is shown as a solid green line (green dashed for PN and cyan dashed for MOS).

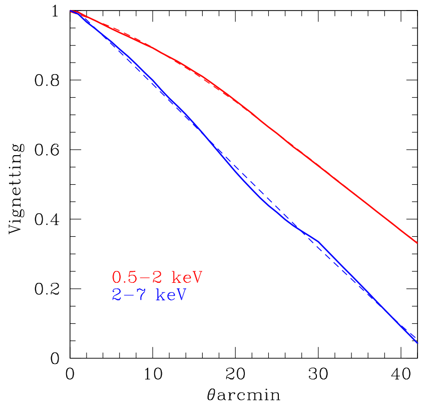


**Fig. 2.** Vignetting with respect to the aimpoint as a function of the off-axis angle at 1 keV (red solid line) and 4 keV (blue solid line). Dashed lines show the analytical fits used in the simulations.

| Source | 0.5 – 2 keV | 2 – 7 keV |
|---|---|---|
| XRB, $\Gamma = 1.4$ | $2.25 \times 10^{-13}$ | $2.35 \times 10^{-12}$ |
| AGN z=1, $N_H = 10^{21}$ | $2.19 \times 10^{-13}$ | $2.06 \times 10^{-12}$ |
| AGN z=1, $N_H = 10^{23}$ | $3.45 \times 10^{-13}$ | $2.40 \times 10^{-12}$ |
| SF Gal $\Gamma = 1.9$ | $2.16 \times 10^{-13}$ | $2.05 \times 10^{-12}$ |
| ICM $z = 0.5, kT = 5$ | $2.22 \times 10^{-13}$ | $1.85 \times 10^{-12}$ |

**Table 1.** Typical Energy Conversion Factors (ECF) at the aimpoint. The units are erg s$^{-1}$ cm$^{-2}$/(cts s$^{-1}$). We assume a typical Galactic absorption of $N_H = 3 \times 10^{20}$ cm$^{-2}$.

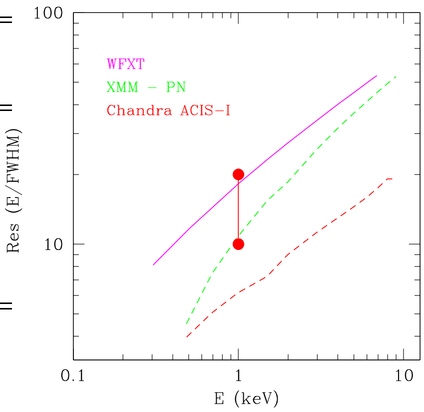


**Fig. 3.** Spectral resolution $E/\Delta E$ for WFXT (magenta solid line). Goal and requirement are shown as red dots. Spectral resolution for the XMM PN detector is shown in green, while the Chandra ACIS-I in red.

ability to measure the ubiquitous Fe $K_\alpha$ line in the ICM spectra is one of the key requirements in order to build a cosmological sample of groups and clusters of galaxies without recurring to time–expensive optical follow-up (see §5).

An important figure which is obtained directly from the WFXT spectral response, is the Energy Conversion Factor (ECF) appropriate to a given spectral shape (i.e., a given source class). The ECFs are defined as the ratio of the observed energy flux in a given band and the observed photon rate in the same band, and are computed always at the aimpoint (so they must be weighted by the vignetting whenever the observed source is not at the aimpoint). In Table 2 we show the conversion factors for some typical extragalactic source in the soft and hard bands. These values are posted here as a reference: in the simulations the net photon rate of each source is computed exactly according to its spectral shape.

The next aspect we consider is the noise, which is due to the sum of several components. One is the particle (or instrumental) background, while the other contributions are from astrophysical sources. The galactic foreground is truly diffuse, with fluctuations of the order of a few percent. The extragalactic unresolved background is given by undetected point sources and it depends on the flux limit at which the extragalactic sources can be resolved, and therefore it is also a function of the exposure time. In our simulator we include the unresolved AGN contribution and the unresolved ICM contribution as a uniform distribution spread across the FOV. As a useful reference we show the expected average values in Table 2 in photons per second per field of view (one square degree). The particle background is very low thanks to the low Earth orbit proposed for WFXT. The Galactic background is by far the dominant component in the soft band (actually below 1 keV), while the extragalactic background, due to point sources (mostly AGN) and groups and clusters, strongly depends on the different exposure of the Wide, Medium and Deep surveys, given the different minimum flux at which it is possible to detect single sources.

The information given so far can be used to estimate the collected photons from several extragalactic sources in each of the three WFXT planned surveys. However, a proper estimate of the detectability, or the signal-to-noise ratio, of each source, depends also on the PSF. Thanks to the polynomial X-ray mirrors (Burrows et al. 1992) the PSF has an HEW of 5 arcsec almost constant across the entire field of view. This is the key property which makes WFXT the ultimate X-ray survey mission, since it allows one to detect and characterize pointlike and extended sources without hitting source–confusion down to very low fluxes. Together with the hard band sensitivity, the spatial resolution constitute the main difference of WFXT with respect to other planned X-ray missions like eRosita (Predehl et al. 2010).

| Source | 0.5 – 2 keV | 2 – 7 keV |
|---|---|---|
| Particles | 0.188 | 0.397 |
| Galactic | 21.4 | 0.0 |
| AGN wide | 9.5 | 3.13 |
| AGN medium | 3.9 | 1.65 |
| AGN deep | 0.8 | 0.17 |
| Cluster wide | 1.46 | 0.3 |
| Cluster medium | 0.79 | 0.14 |
| Cluster deep | 0.2 | 0.03 |

**Table 2.** Total background photon rates (cts/s) in the soft and hard bands for one FOV (1 $\mathrm{deg}^2$)

A realistic image simulator needs a detailed modelling of the PSF. The HEW of the PSF is shown in Figure 4, at two different energies, 1 and 4 keV, representative of the soft and hard bands. Note that the images are realized taking into account all the features of the PSF, including its asymmetric shape (Conconi et al. 2010).

This short review of the WFXT instrumental properties is sufficient to comprehend the main ingredients of the WFXT mock images we realized. In order to achieve a realistic rendition of the X-ray sky, we now exploit what we have learned from deep X-ray extragalactic surveys to date on different source populations.

## 3. Source populations in extragalactic fields

In this work, we present only single–pointing images of extragalactic fields. The point source populations include four families of Active Galactic Nuclei (Unabsorbed, Compton–Thin, Mildly Compton–Thick and Heavily Compton–Thick), and normal and star forming galaxies, consistently with the observed luminosity function and extrapolated to high redshifts according to the Gilli et al.

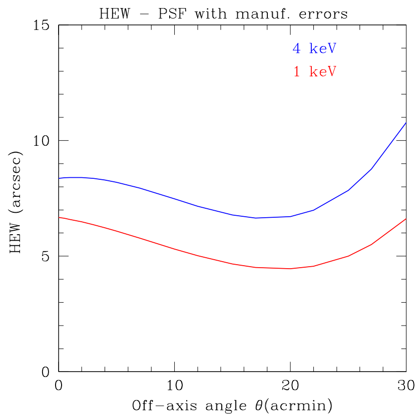


**Fig. 4.** Half Energy Width of the PSF (including estimated manufacturing errors) in the soft (1 keV, red line) and hard band (4 keV, blue line) as a function of the off–axis angle $\theta$.

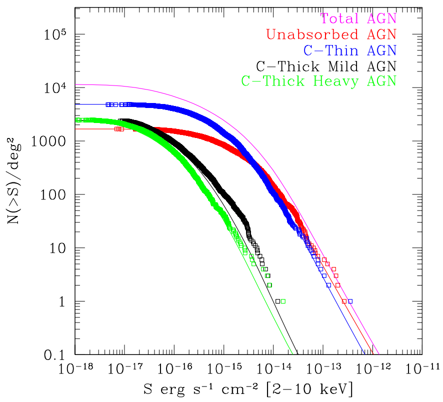


**Fig. 5.** The hard-band logNlogS from the mock input catalog of extragalactic point sources (empty squares) compared with the input model by Gilli et al. (2007) (solid lines). The contributions of unabsorbed, Compton-Thin and Compton-Thick AGN are plotted separately.

(2007) XRB synthesis model. The input logN-logS are shown in Figure 5. Two spectra of a Compton Thin and a Compton Thick AGN, as observed by WFXT, are shown in Figure 6. Each AGN type is simulated with a neutral Iron $K_\alpha$ line at 6.4 keV rest-frame with a typical equivalent width as commonly observed in each source class, as shown in Figure 7. The presence of the Iron line allows one to measure the redshift for a significant number of AGN, even though its equivalent width is expected to vary significantly from source to source. The feature at 2 keV in the spectra is due to a dip in the effective area (compare with Figure 1).

In addition to AGN, another important class of point sources is constituted by the star-forming galaxies. As we learned from the Chandra Deep Fields (Norman et al. 2004; Lehmer et al. 2008), star forming galaxies are expected to dominate the number counts below fluxes $\sim 10^{-17}$ cgs. WFXT will not reach fluxes lower than the limits achieved in the Chandra Deep Fields, however it will be able to detect thousands of star forming galaxies up to reshift one, providing an unbiased view of the cosmic star formation history with an unprecedented statistics (see contribution by P. Ranalli in this volume). We extract the galaxy catalog from the soft logN-logS relations (Ranalli et al. 2005). For all the galaxies we assumed an intrinsically unabsorbed power law spectrum with photon index $\Gamma = 2$.

Another important class of extragalactic sources are groups and clusters of galaxies. These sources are intrinsically extended since the X-ray emission is due to the thermal bremsstrahlung in the hot ICM. We extracted a population of groups and clusters from the Press & Schechter (1974) mass function, tuning the cosmological parameters in a ΛCDM universe in order to reproduce with reasonable accuracy the existing constraints on the observed number counts (see Figure 8) and the observed luminosity (Rosati et al. 1998) and temperature functions (Henry et al. 2009). Given their nature, X-ray extended sources have a variety of different morphologies and concentrations, which will be resolved in most cases thanks to the WFXT angular resolution. In order to render this aspect in our simulations, we used real Chandra images (i.e., at very high resolution) from a representative lo-

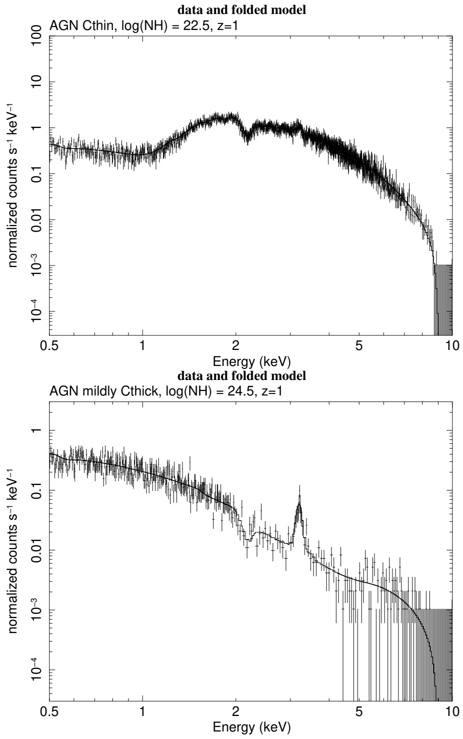


**Fig. 6.** Top panel: the spectrum of a typical compton-Thin AGN at z=1 with intrinsic absorption $log(N_H) \sim 22.5$ cm$^{-2}$ and flux $F_S \sim 5 \times 10^{-14}$ erg s$^{-1}$ cm$^{-2}$ observed for 13.2 ks with WFXT. Bottom panel: the spectrum of a mildly Compton Thick AGN at z=1 with nominal intrinsic absorption $log(N_H) \sim 24.5$ cm$^{-2}$, soft flux $\sim 5.4 \times 10^{-14}$ erg s$^{-1}$ cm$^{-2}$, observed for 13.2 ks with WFXT. In both cases a soft scattered component in addition to the primary absorbed one has been considered.

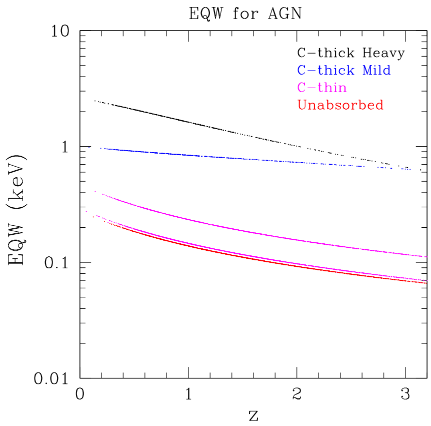


**Fig. 7.** Observed-frame equivalent width of the 6.4 keV neutral Fe $K_\alpha$ line adopted in our AGN population for different AGN types, as a function of redshift.

cal sample of groups and clusters in order to mimic the observed mix of flat and strongly peaked surface brightness profiles (see Figure 9). This procedure has been adapted from the cloning technique described in Santos et al. (2008). The presence of a cool–core may affect the detectability of the cluster emission particularly at high redshift, and therefore it will be an important aspect when quantifying the completeness of deep cluster samples. Clearly, some uncertainty is due to the evolution of cool-cores, which is currently measured to be mild (Santos et al. 2010). At present, we simply assume a fair mix of cool-core and non cool-core clusters as observed locally.

The WFXT images are created in three bands (0.5-1 keV, 1-2 keV, and 2-7 keV) and combined to produce color images (see Figure 10). We also produce the soft image (0.5-2 keV band) which will be used for source detection, together with the 2-7 keV hard band image. Each image is given by the sum of the three modules. The original pixel size is assumed to be 0.88 arcsec, while the final images are resized by a factor of three (corresponding to a pixel of 2.64 arcsec) thus adequately sampling the PSF across the FOV.

We showed the efficiency of WFXT by comparing one tile of the medium survey (corresponding to a single pointing of WFXT with a 13.2 ks exposure) with the Chandra image of the COSMOS field (Cappelluti et al. 2009) in the contribution by Rosati et al., this volume. The striking result is that WFXT is $\sim 150$ times faster in obtaining an image of the same solid angle and same depth of Chandra COSMOS, and with a resolution only a factor of two below that of the Chandra mosaic. This direct comparison shows the tremendous survey efficiency of WFXT.

**Fig. 10.** A simulated WFXT extragalactic field with an exposure of 13.2 ks (corresponding to one tile of the Medium survey).

## 4. Source detection with WFXT

In principle, the large size of the WFXT images and the large number of sources which will be detected would require dedicated software. Indeed, we are planning to develope specific source detection algorithms and source extraction procedures in the next future. For the purpose of this Paper, we use the algorithm *wavdetect* which has been developed for Chandra and it is part of the `ciao` software. This procedure, despite not optimized for WFXT data, allows us to perform a rapid test on the quality of our simulated images.

We run `wavdetect` on the soft (0.5-2 keV) and hard (2-7 keV) images of a tile of the Medium survey (corresponding to an exposure time of 13.2 ks) with a standard set of parameters. The catalog of the detected sources is then matched with the input sources. In this way we have a catalog of the matched sources, a list of spurious and a list of undetected sources.

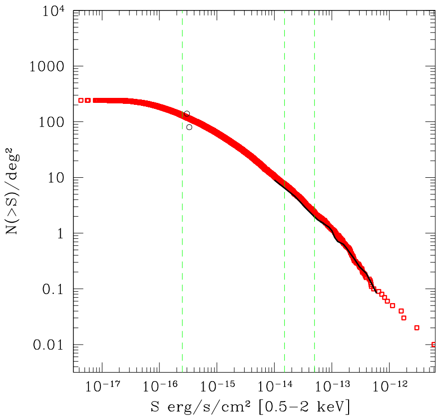


**Fig. 8.** Soft band logN-logS for groups and clusters of galaxies from the input catalog of 100 square degrees (corresponding to 100 WFXT fields), extracted from the PS-like mass function model (red squares). The black line refers to the ROSAT Deep Cluster Survey (RDCS) by Rosati et al. (1998). The two circles at low fluxes refer to the Chandra Deep Fields (Rosati et al. 2002). Vertical dashed lines show the approximate flux limits for detection corresponding to the three WFXT surveys.

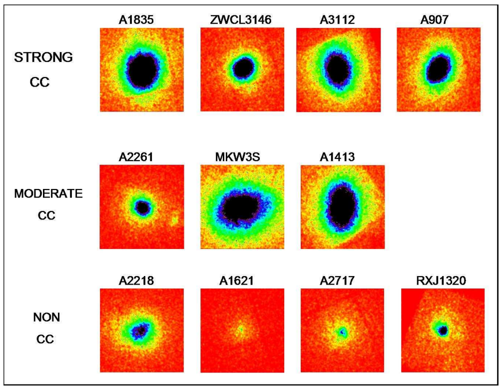


**Fig. 9.** Cluster templates (original Chandra images) used in the simulations, representing three classes with different cool-core strength (Santos et al. 2008).

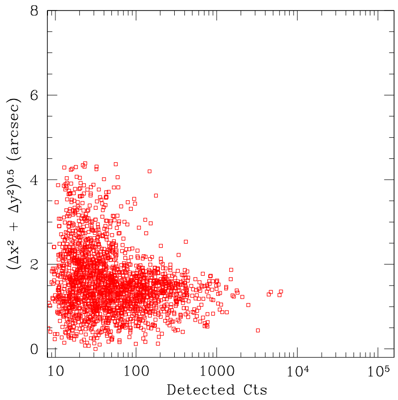


**Fig. 11.** Position error in arcsec as a function of the net detected counts for point sources, from a simulated soft band image of the Medium survey (13.2 ks).

Point sources are recovered with a position accuracy typically below 2 arcsec (see Figure 11). Note that part of this error is due to the asymmetry of the PSF, which is not corrected here, but it can be accounted for when the PSF model will be included in the detection algorithm. The number of detected photons for each source is in very good agreement with the input value within the poissonian error (see Figure 12). The sources are recovered efficiently down to 20 net photons, a value below which the number of undetected sources grows rapidly (see Figure 13). This value provide a very conservative estimate of the flux limit in WFXT images, and it can be considered constant with respect to the exposure time, since point sources are very mildly affected by the diffuse background. For an image of the Medium survey, 20 net photons correspond to a flux of $3.3 \times 10^{-16}$ erg s$^{-1}$ cm$^{-2}$ in the soft band. At the same time, thanks to the low background, the number of spurious sources is negligible above 20 counts. We conclude that the constant PSF of WFXT allows one to detect sources with an almost flat sky coverage and negligible contamination down to very low flux levels. Eventually, it will be possible to decrease the detection limit by a factor of two with a more sophisticated detection algorithm.

The detected photons are in agreement with the input value also for extended sources

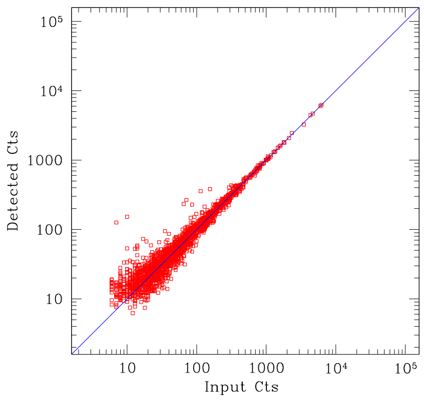


**Fig. 12.** Recovered vs input counts in the soft band for point sources (from a simulated soft band image of the Medium survey).

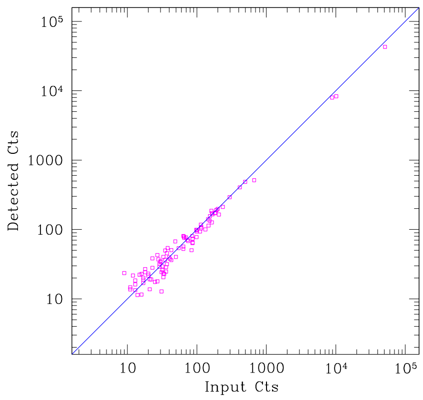


**Fig. 14.** Recovered vs input counts in the soft band for extended sources (from a simulated soft band image of the Medium survey).

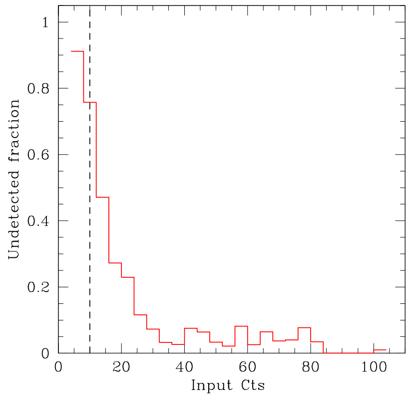


**Fig. 13.** Histogram distribution of the undetected point sources in the soft band as a function of the input photons (from a simulated image of the Medium survey).

(groups and clusters of galaxies) once a small offset due to the lost emission at low surface brightness is accounted for. However, at present, our schematic detection algorithm is not efficient in characterizing extended sources. Therefore, we set a conservative detection limit by requiring a typical S/N ratio of 5 from aperture photometry. To do this, we assume that for a typical group or cluster at medium and large redshifts, roughly 80% of the flux is included within 30 arcsec, corresponding to an extraction area of $A_{ext} = 2.18 \times 10^{-4}$ deg$^2$. We adopt an average conversion factor of $2.2 \times 10^{-13}$ erg s$^{-1}$ cm$^{-2}$ for a typical ICM emission as in Table 2, and we use the background values shown in Table 2. We compute the S/N ratio as follows:

$$BCK = BCK_{rate} \times T_{exp} \times A_{ext} \,, \quad (1)$$

$$S/N = CTS_{net} / \sqrt{CTS + 2\,BCK} \,. \quad (2)$$

Requiring $S/N > 5$, the condition on the minimum number of net detected photons within the extraction regions is:

$$CTS_{det} = 12.5 \times (1 + \sqrt{1 + 0.32 \times BCK}) \,, \quad (3)$$

corresponding to a flux of $F_{det} = CTS_{det} \times ECF/T_{exp}/0.8$, where the factor of 0.8 accounts for the lost flux (see Table 3).

## 5. Redshift measure via X-ray spectroscopy of distant clusters

Now we focus on the properties of the WFXT sample of X-ray clusters. As we showed in this

| Survey | $CTS_{ext}$ | $CTS_{tot}$ | $F_{lim}/10^{-15}$ |
|---|---|---|---|
| Wide | 39.4 | 49.3 | 5.42 |
| Medium | 69 | 86.1 | 1.44 |
| Deep | 294 | 367 | 0.2 |

**Table 3.** Detection limits for extended sources: $CTS_{ext}$ is the minimum number of detected photons in the extraction regions, $CTS_{tot}$ is the detection limit in terms of total emitted photons, and $F_{lim}$ is the total flux limit.

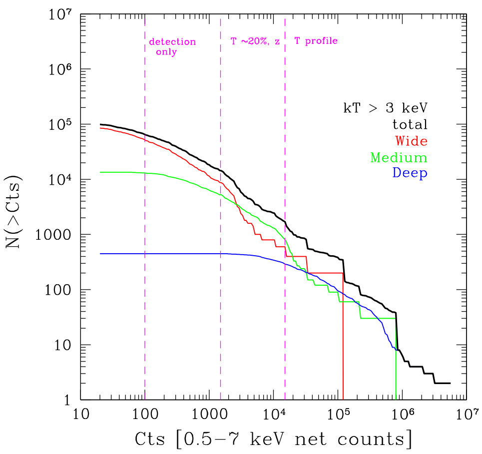


**Fig. 15.** Number of clusters with $kT > 3$ keV for the three WFXT surveys as a function of the detected photons (0.5-7 keV band). Vertical dashed lines correspond roughly to the average detection limit (100 photons), to the limit for spectral analysis (1500 net photons) and the the limit for spatially resolved spectral analysis (15000 net photons).

work, all the properties of the WFXT concur to deliver a very high quality set of data: the large effective area provides a high number of detected photons for sources down to low fluxes; the angular resolution allows us to avoid source confusion and remove the contribution of point sources from the diffuse emission of clusters and groups; finally the large field of view allows one to collect a large number of sources in a reasonable amount of time. To quantify the expected sample of clusters with $kT > 3$ keV from the three WFXT surveys, we show in Figure 15 the number of extended sources as a function of the detected photons.

Despite the bulk of the detected photons will be in the soft band, the relatively high effective area in the hard band (2-7 keV) will allow us to measure the ICM temperature and detect the $K_\alpha$ Fe line at any redshift whenever the equivalent width is $few \times 100$ eV. For the first time, this opens the possibility of building a sample of clusters with measured redshifts without recurring to time-consuming optical follow-up work.

To explore this relevant science case, we performed spectral simulations of a sample of groups and clusters extracted from the Press & Schechter (1974) mass function, whose temperatures and luminosities are assigned according to the observed *M*-*T* and *L*-*T* relations. The X-ray spectra are analyzed with `Xspec` with a `mekal` model where the redshift is left free to vary. Even though the Fe $K_\alpha$ line complex is ubiquitous in the ICM emission, the blind search of the Fe line is a difficult task. The background and the poisson noise in the rapidly decreasing signal in the hard band, may originate spurious lines which lead to catastrophic errors on the measured X-ray redshift. Another source of uncertainty is the intrinsic Fe abundance, which is significantly varying particularly in groups. Our automatic procedure to find the X-ray redshift (Yu et al. 2010, in preparation) shows that we will be able to detect the Fe $K_\alpha$ line complex in any extended source detected with more than 800 total photons. The number of catastrophic failures ($\Delta z \geq 0.1$) is kept low, and the typical error on the redshift is $\langle \Delta z \rangle \sim 0.022$. This can be seen in Figure 16.

The occurrence of catastrofic errors depends strongly on the total detected photons, and mildly on the intrinsic Fe abundance. As shown in Figure 17, where only clusters with more than 800 detected photons are considered, we can conservatively adopt a lower limit of 1500 net detected photons above which we can rely on the X-ray measured redshift. We can straightforwardly compute that the three

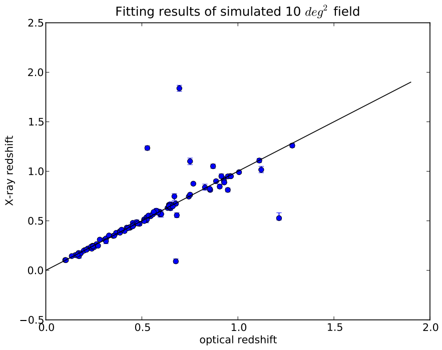


**Fig. 16.** X-ray measured redshift vs optical (input) redshift from the spectral analysis of a mock simulation of 10 square degrees of the Medium survey (exposure time of 13.2 ks). Vignetting effects are included (from Yu et al. 2010).

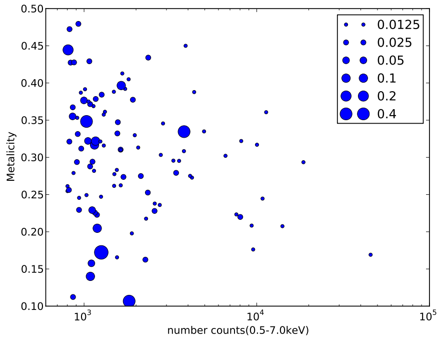


**Fig. 17.** Input Fe abundance vs detected number counts for the mock simulation of 10 square degrees of the Medium survey. The size of each dot is proportional to the error $\Delta z$ with respect to the input value (from Yu et al. 2010).

WFXT planned surveys will provide a total of 15000-20000 clusters with $kT > 3$ keV (as shown in Figure 15) with measured X-ray redshift, a *golden sample* that can be directly used for precision cosmological tests with an unprecedented statistics (see Borgani et al. this volume).

## 6. Conclusions

The Wide Field X-ray Telescope has been designed in order to be optimized for surveys. Its goal is not only to detect the largest number of X-ray sources, but also to characterize them in order to address several science cases. The superiority of WFXT as an X-ray survey machine, is due to the combination of angular resolution ($HEW \sim 5$ arcsec), high effective area, and good sensitivity in the hard band. These properties open the discovery space of many scientific cases that are not addressed by any other present of future X–ray mission.

Thanks to the detailed imaging and spectral simulations presented in this work, we have investigated, among the many scientific cases within reach of WFXT, the construction of a cluster sample as large as 15000-20000 with redshift measured from the X-ray spectra, suitable for high precision cosmological tests. WFXT is therefore in the position of achieving the maximum scientific impact thanks to the high–quality characterization of the detected sources, of providing an extremely large number of targets suitable for next-generation X-ray missions like the International X-ray Observatory (IXO), with a unique legacy value to be added to the next–generation wide field surveys at other wavelengths.

The simulation tool presented in this work will provide an important testbed to refine the design of the mission in keeping with the scientific requirements. In particular, the imaging and spectral simulations will be used to develop specific detection algorithms and to refine analysis procedures. On the basis of the end-to-end analysis presented here, we reinforce our idea that an X-ray mission optimized for surveys like WFXT is necessary to bring X-ray astronomy at the level of the optical, IR, submm and radio wavebands as foreseen in the coming decade.

*Acknowledgements.* We acknowldge support under the ASI grant I/088/06/0 and the INFN PD51 grant.

## References

Burrows, C. J., Burg, R., & Giacconi, R. 1992, ApJ, 392, 760

Cappelluti, N., Brusa, M., Hasinger, G., et al. 2009, A&A, 497, 635

Conconi, P., Campana, S., Tagliaferri, G., et al. 2010, MNRAS, 405, 877

Giacconi, R., Borgani, S., Rosati, P., et al. 2009, in ArXiv Astrophysics e-prints, Vol. 2010, astro2010: The Astronomy and Astrophysics Decadal Survey, 90

Gilli, R., Comastri, A., & Hasinger, G. 2007, A&A, 463, 79

Henry, J. P., Evrard, A. E., Hoekstra, H., Babul, A., & Mahdavi, A. 2009, ApJ, 691, 1307

Lehmer, B. D., Brandt, W. N., Alexander, D. M., et al. 2008, ApJ, 681, 1163

Murray, S., Gilli, R., Tozzi, P., et al. 2009, in ArXiv Astrophysics e-prints, Vol. 2010, astro2010: The Astronomy and Astrophysics Decadal Survey, 217

Murray, S., Norman, C., Ptak, A., et al. 2008, in Society of Photo-Optical Instrumentation Engineers (SPIE) Conference Series, Vol. 7011, Society of Photo-Optical Instrumentation Engineers (SPIE) Conference Series

Norman, C., Ptak, A., Hornschemeier, A., et al. 2004, ApJ, 607, 721

Predehl, P., Böhringer, H., Brunner, H., et al. 2010, in American Institute of Physics Conference Series, Vol. 1248, American Institute of Physics Conference Series, ed. A. Comastri, L. Angelini, & M. Cappi, 543–548

Press, W. H. & Schechter, P. 1974, ApJ, 187, 425

Ptak, A., Feigelson, E., Chu, Y., et al. 2009, in ArXiv Astrophysics e-prints, Vol. 2010, astro2010: The Astronomy and Astrophysics Decadal Survey, 240

Ranalli, P., Comastri, A., & Setti, G. 2005, A&A, 440, 23

Rosati, P., Borgani, S., & Norman, C. 2002, ARA&A, 40, 539

Rosati, P., della Ceca, R., Norman, C., & Giacconi, R. 1998, ApJ, 492, L21+

Santos, J. S., Rosati, P., Tozzi, P., et al. 2008, A&A, 483, 35

Santos, J. S., Tozzi, P., Rosati, P., & Boehringer, H. 2010, ArXiv e-prints

Vikhlinin, A., Murray, S., Gilli, R., et al. 2009, in Astronomy, Vol. 2010, AGB Stars and Related Phenomenastro2010: The Astronomy and Astrophysics Decadal Survey, 305